PNAS
www.pnas.org

Supplementary Information for

Disrupted *Cacna1c* Gene Expression Perturbs Spontaneous Ca^{2+} Activity Causing Abnormal Brain Development and Increased Anxiety

Erik Smedler, Lauri Louhivuori, Roman A. Romanov, Débora Masini, Ivar Dehnisch Ellström, Chungliang Wang, Martino Caramia, Zoe West, Songbai Zhang, Paola Rebellato, Seth Malmersjö, Irene Brusini, Shigeaki Kanatani, Gilberto Fisone, Tibor Harkany, and Per Uhlén

Corresponding authors: Erik Smedler and Per Uhlén
Email: erik.smedler@gu.se and per.uhlen@ki.se

This PDF file includes:

Supplementary text
Figures S1 to S8
Tables S1
Legends for Movies S1 to S3
SI References

Other supplementary materials for this manuscript include the following:

Movies S1 to S3

Supplementary text

Supplementary methods

The computational model is based on *N* individual and interconnected cells,

indexed $i, j \in \{1{:}\,N\}, i \neq j$.

1) $C_m \frac{dV_m^i}{dt} = I_{app} - g_K w(V_m^i - V_K) - g_{Ca} m_\infty (V_m^i - V_{Ca}) - \sum_{i=1}^{N} C(i,j) g_{gap} \left(V_m^i - V_m^j\right)$

2) $\frac{dw^i}{dt} = \varphi \frac{w_\infty - w^i}{\tau}$

3) $\frac{d[Ca^{2+}]_{cyt}^i}{dt} = f_{cyt}[-\frac{\frac{3}{r^i}}{2F} g_{Ca} m_\infty (V_m^i - V_{Ca}) - J_{PMCA} + (v_{RYR} P_{RYR} + v_{leakER})\left([Ca^{2+}]_{ER}^i - [Ca^{2+}]_{cyt}^i\right) - J_{SERCA} + \sum_{i=1}^{N} (C(i,j) v_{gap} \left(\frac{r^j}{r^i}\right)^3 [Ca^{2+}]_{cyt}^j - [Ca^{2+}]_{cyt}^i)]$

4) $\frac{d[Ca^{2+}]_{tot}^i}{dt} = f_{cyt}[-\frac{\frac{3}{r^i}}{2F} g_{Ca} m_\infty (V_m^i - V_{Ca}) - J_{PMCA}]$

5) $[Ca^{2+}]_{ER}^i = \frac{[Ca^{2+}]_{tot}^i - [Ca^{2+}]_{cyt}^i}{\sigma}$

The connection between cells *i* and *j* is described by the matrix *C*.

$$C = \begin{pmatrix} C(1,1) & \cdots & C(1,N) \\ \vdots & \ddots & \vdots \\ C(N,1) & \cdots & C(N,N) \end{pmatrix}, \text{ where } C(i,j) = \begin{cases} 1 \leftrightarrow i,j \text{ connected} \\ 0 \leftrightarrow i,j \text{ disconnected} \end{cases}$$

The plasma membrane potential oscillator is described by the Morris-Lecar model (1).

$$m_\infty = 0.5[1 + \tanh(\frac{V_m^i - V_1}{V_2})]$$

$$w_\infty = 0.5[1 + \tanh(\frac{V_m^i - V_3}{V_4})]$$

$$\tau = \frac{1}{\cosh(\frac{V_m^i - V_3}{2V_4})}$$

The plasma membrane Ca^{2+}-ATPase (PMCA) and sarco/endoplasmic reticulum Ca^{2+}-ATPase (SERCA) are described by Hill functions (1).

$$J_{PMCA/SERCA} = \frac{v_{max,PMCA/SERCA}[Ca^{2+}]^2_{cyt}}{K^2_{1/2,PMCA/SERCA} + [Ca^{2+}]^2_{cyt}}$$

The ryanodine receptor (RyR) is described by Keizer and Levine (2) using a quasi-steady-state approximation (1).

$$P_{RyR} = n_\infty \frac{1 + (\frac{[Ca^{2+}]^i_{cyt}}{K_b})^3}{1 + (\frac{K_a}{[Ca^{2+}]^i_{cyt}})^4 + (\frac{[Ca^{2+}]^i_{cyt}}{K_b})^3}$$

$$n_\infty = \frac{1 + (\frac{K_a}{[Ca^{2+}]^i_{cyt}})^4 + (\frac{[Ca^{2+}]^i_{cyt}}{K_b})^3}{1 + \frac{1}{K_c} + (\frac{K_a}{[Ca^{2+}]^i_{cyt}})^4 + (\frac{[Ca^{2+}]^i_{cyt}}{K_b})^3}$$

Supplementary results

The computational model was based on three cells interconnected with gap junctions permeable to both electrical current and calcium ions (Ca^{2+}) to varying degrees. Each individual cell was given its own time-dependent membrane potential (V_{PM}), cytosolic Ca^{2+} concentration ($[Ca^{2+}]_{cyt}$), and endoplasmic reticulum (ER) Ca^{2+} concentration ($[Ca^{2+}]_{ER}$). The mobilization of Ca^{2+} within each cell was handled by typical Ca^{2+} transporters. The transport of Ca^{2+} into and out of the ER stores occurred through the SERCAs and RyRs, respectively. The passage of Ca^{2+} across the plasma membrane occurred through the PMCAs and voltage-gated Ca^{2+} channels (VGCCs). The membrane potential was dependent on the VGCCs and voltage-dependent potassium (K^+) channels (I_K). We did not include voltage-dependent sodium (Na^+) channels in the model since experimental data from neural progenitor cells show that spontaneous Ca^{2+} activity is not blocked by Na^+ channel inhibition (3). The VGCC was given the kinetics of an L-type Ca^{2+} channel with an activation voltage around the resting potential of -3 mV (*SI Appendix*, Fig. S1*A*). Electrophysiology

recordings show that the activation voltage of L-type VGCCs is -17.6 mV (4). We also included an experimentally applied current (I_{app}) in our equations that could be used to validate the results from our computational model with the results from patch-clamp recordings. The model assumed spherical and well-stirred cells, fast Ca^{2+} buffers, and fast activation of VGCCs compared to K^+ channels.

When we assigned the relevant experimental values to the parameters of our computational model (*SI Appendix*, Table S1), we observed spontaneous Ca^{2+} oscillations of 6 mHz (period T = 167 s) with a FDHM of ~70 s (Fig. 2*B*). These results were consistent with the experimental data from Ca^{2+} recordings in neural progenitor cells showing ~5 mHz and 45 s (3). The experimental data also showed that the membrane potential oscillated considerably faster than the cytosolic Ca^{2+} concentration, at ~900 mHz versus ~5 mHz (3). The 180 times faster membrane potential oscillation is similar to the theoretical membrane potential oscillation, which oscillates 167 times faster (1000 mHz versus 6 mHz) than the cytosolic Ca^{2+} concentration. When the gap junction Ca^{2+} permeability was set to zero, unsynchronized signals were displayed, indicating that the Ca^{2+} level in a cell strongly affects the Ca^{2+} level in adjacent cells (*SI Appendix*, Fig. S1*E*). Calculation of the Pearson's correlation coefficient r between a pacemaker cell and an adjacent cell confirmed that increasing the Ca^{2+} permeability of the gap junctions synchronized the signals in adjacent cells (*SI Appendix*, Fig. S1*F*).

To assess the validity of our theoretical model, we inhibited ion transporters and compared the results with experimental data. The inhibition of RyRs blocked the Ca^{2+} oscillations both in the computational model and in experiments on neural progenitors (*SI Appendix*, Fig. S2*A*) but did not block membrane potential oscillations. The blockade of VGCCs abolished the spontaneous Ca^{2+} oscillations and membrane potential oscillations in both systems (*SI Appendix*, Fig. S2*B*). The inhibition of SERCA pumps only blocked the Ca^{2+} oscillations in the theoretical model and not in the experiments (*SI Appendix*, Fig. S2*C*). The membrane potential oscillations were not blocked by SERCA inhibition. Interestingly, previous experiments also showed that spontaneous Ca^{2+} activity

in neural progenitor cells persists upon SERCA inhibition with CPA or thapsigargin (3). A possible explanation for the discrepancy between the computational model and the experimental results may be incomplete pharmacological inhibition of SERCA. While testing this hypothesis, we observed that partial inhibition of SERCA reduced the amplitude of the spontaneous Ca^{2+} oscillations (*SI Appendix*, Fig. S2*D*). Notably, SERCA inhibition also decreased the amplitude of spontaneous Ca^{2+} oscillations in the experiments (*SI Appendix*, Fig. S2*C*), suggesting that 1 μM thapsigargin could not completely inhibit the SERCA pump. Our theoretical model showed that 65% SERCA inhibition was sufficient to entirely abolish the spontaneous Ca^{2+} oscillations (*SI Appendix*, Fig. S2*E*). Together, this set of experiments demonstrated the accuracy of our theoretical model and that spontaneous Ca^{2+} activity requires spontaneous membrane potential oscillations and not *vice versa*.

To determine the oscillatory regime, we performed a bifurcation analysis (5). Bifurcation analysis is a powerful tool to study the dynamics of nonlinear systems (6). We chose to study Hopf bifurcation points as they describe a critical point where a system's stability switches and a periodic solution arises (5). By varying either the gap junction conductance or the VGCC conductance while keeping the other constant, oscillatory regimes emerged that were delimited by Hopf bifurcation points (*SI Appendix*, Fig. S3 *A*–*D*). These Hopf bifurcations were classified as supercritical since the amplitudes of the function gradually increased (7). Treating the RyR permeability to Ca^{2+} as a bifurcation parameter once again showed that the spontaneous Ca^{2+} oscillations were driven by membrane potential oscillations and not *vice versa* (*SI Appendix*, Fig. S3*E*). While varying the RyR permeability to Ca^{2+} in the pacemaker cells, the Ca^{2+} activity was measured in either the pacemaker (blue trace) or nonpacemaker cell (red trace). The nonpacemaker cell was unaffected by increases or decreases in the RyR permeability to Ca^{2+} in the adjacent pacemaker cell, implying that the electrical current was still conducted via gap junctions. However, the pacemaker cell stopped oscillating when the permeability values became too high ($\nu_{RyR} \approx 10^{2}\ s^{-1}$) but contained to oscillate under low permeability values ($\nu_{RyR} \approx 10^{-4}\ s^{-1}$). Under these circumstances, the spontaneous Ca^{2+}

oscillations in the pacemaker cell were driven by the adjacent nonpacemaker cells, which was proven by the finding that the activity vanished upon gap junction inhibition (*SI Appendix*, Fig. S3*F*).

To calculate the percentage of pacemaker cells generated by the computational model, we determined an expression distribution for *Cacna1c*. Since the variances of the RT-qPCR values exceeded the means and could thus not be classified as Poisson (8), we assumed a Gaussian distribution of expression. Using the mean and standard deviation values from the *Cacna1c* RT-qPCR experiments (*SI Appendix*, Fig. S4*G*), we derived a Gauss curve for each day of neural progenitor differentiation (Fig. 3*D*). By combining the *Cacna1c* RT-qPCR measurements for each day with the bifurcation window (Δ = 39%) that enabled spontaneous Ca^{2+} oscillations (*SI Appendix*, Fig. S3*D*), we performed a statistical assumption for the percentage of pacemaker cells from the Gauss distributions (Fig. 3 *D* and *E*). On day 8, when a significant increase in the number of spontaneously active neural progenitor cells was observed, the computational model predicted 20% pacemaker cells (*SI Appendix*, Fig. S4*C*).

Our data generated by the computational model suggested that the only difference between a pacemaker cell and a nonpacemaker cell was the VGCC conductance. To assess the validity of this conclusion, we performed a series of patch-clamp recordings. We first tested whether individual cells in our neural progenitor cell population were excitable or non-excitable (*SI Appendix*, Fig. S5 *C*–*E*). When a current pulse was applied, excitable cells responded with a transient response, whereas non-excitable cells responded with oscillations (*SI Appendix*, Fig. S5 *F*–*H*).

Supplementary Figures

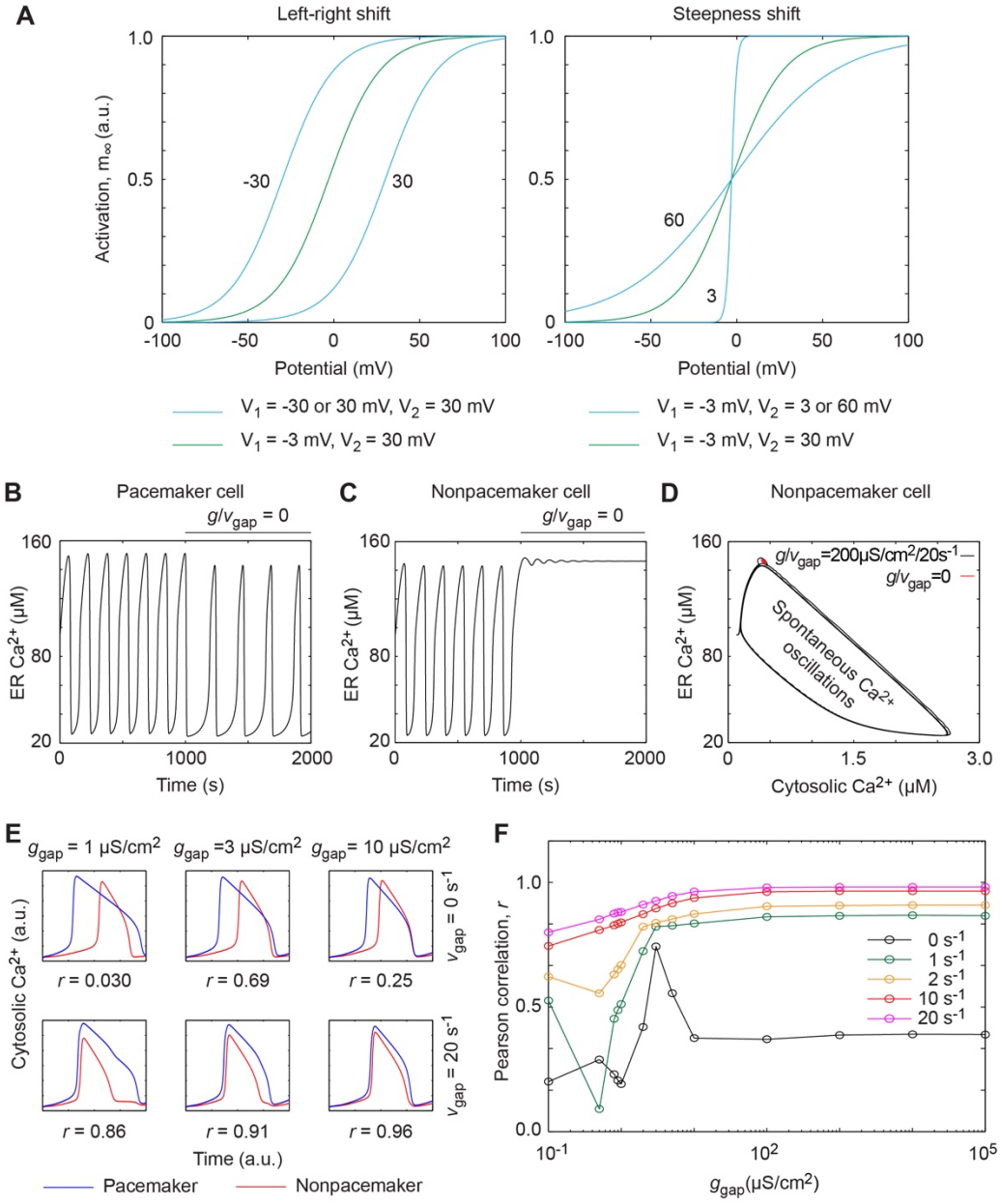

Fig. S1. Modelling the influence of VGCCs and gap junctions on pacemaker and nonpacemaker cells. (*A*) The kinetics of VGCCs in our model. The activation variable as a function of the voltage parameters V_1 (activation voltage) and V_2 (voltage width). (*B and C*) The concentration of Ca^{2+} in the endoplasmic reticulum (ER) in a pacemaker cell (*B*) and nonpacemaker cell (*C*) upon inhibition of gap junctions. (*D*) Phase plot of the Ca^{2+} concentration in the cytosol and ER in a nonpacemaker cell before (black) and after (red) inhibition of gap junctions. (*E*) Cytosolic Ca^{2+} in a pacemaker cell (blue) and nonpacemaker cell (red) at various gap junction Ca^{2+} permeabilities and conductance, as indicated. The Pearson's *r* is stated for each condition. (*F*) The Pearson correlation (*r*) as a function of gap junction Ca^{2+} permeability (g_{gap}) between a pacemaker and nonpacemaker cell.

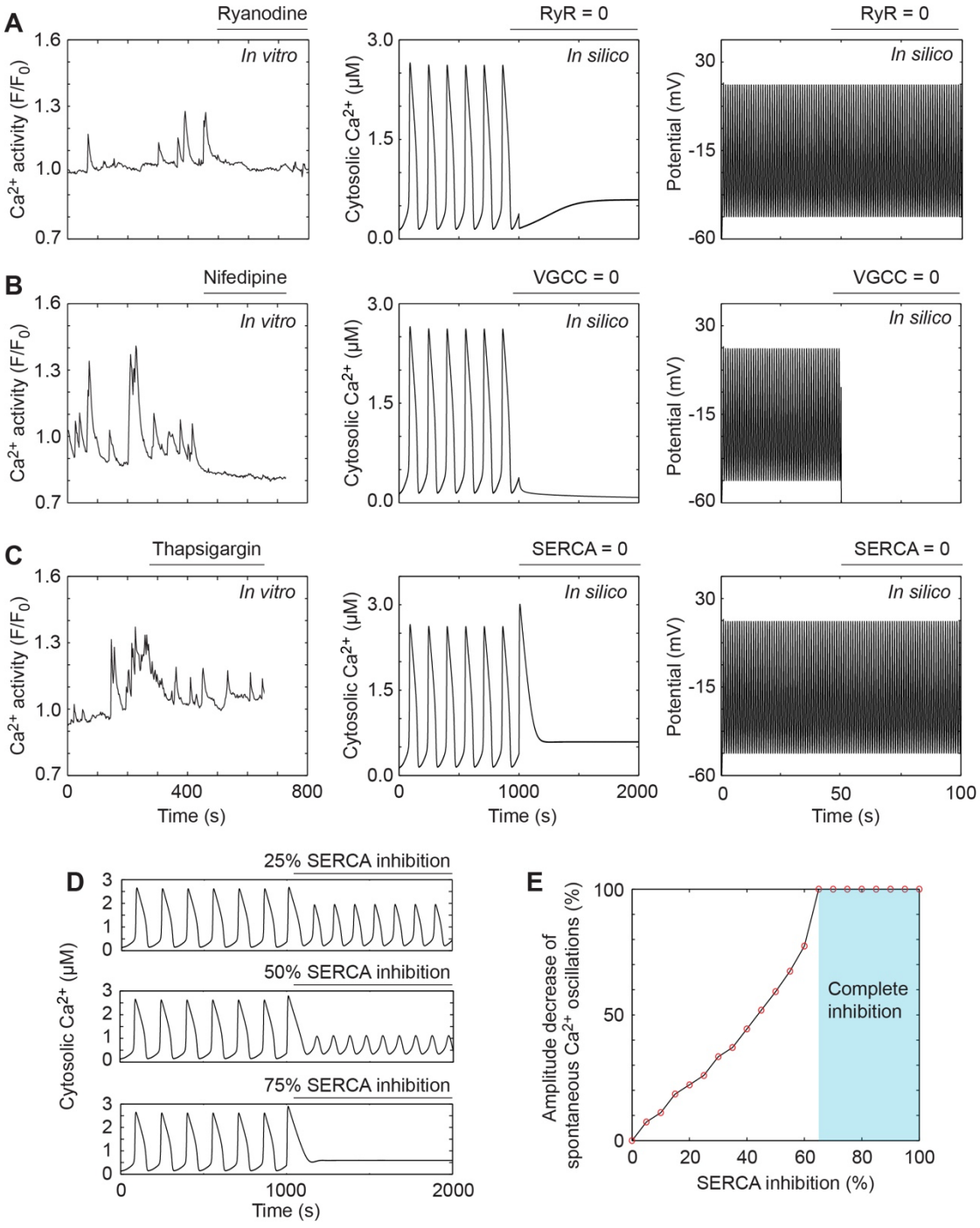

Fig. S2. Modelling the influence of RyR, VGCC, and SERCA inhibition on spontaneous Ca^{2+} oscillations. (*A* to *C*) The effect on spontaneous Ca^{2+} oscillations upon inhibition of RyR with 10 μM ryanodine (*A*), VGCC with 5 μM nifedipine (*B*), and SERCA with 1 μM thapsigargin (*C*). Experimental data from neural progenitor cells are indicated *in vitro* and computational data are indicated *in silico*. (*D*) The effect on spontaneous Ca^{2+} oscillations upon 25%, 50%, and 75% inhibition of SERCA. (*E*) The decrease in amplitude of spontaneous Ca^{2+} oscillations as a function of SERCA inhibition. The blue shaded area indicates complete inhibition of oscillations.

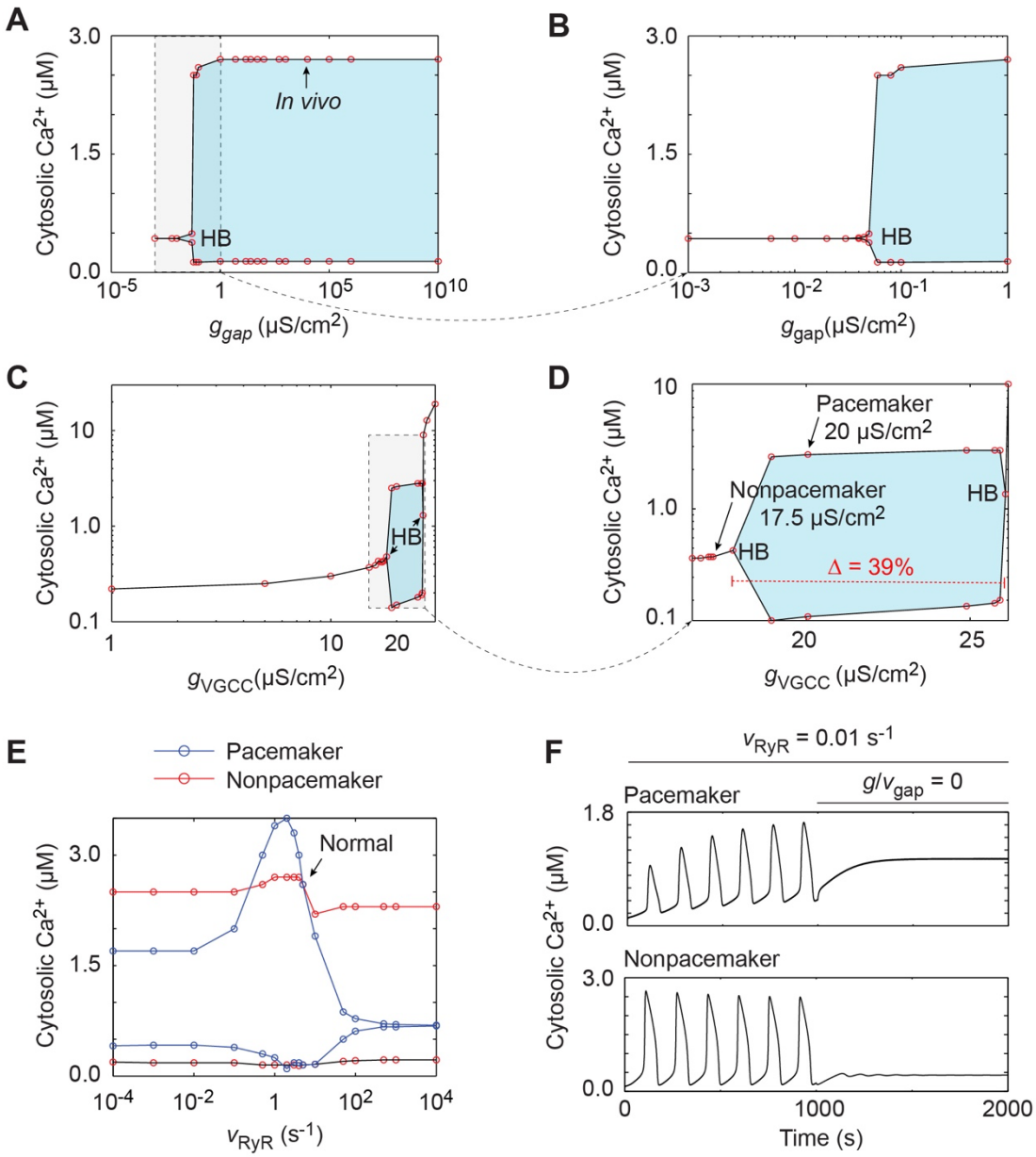

Fig. S3. Bifurcation analyses of gap junction, VGCC, and RyR conductances. (*A*) Bifurcation analysis of the cytosolic Ca^{2+} concentration in a nonpacemaker cell with the gap junction conductance (g_{gap}) as bifurcation parameter when v_{gap} = 0 s^{-1} and g_{VGCC} = 17.5 μS/cm^2. Hopf bifurcation (HB) at g_{gap} = 0.04 μS/cm^2. *In vivo*, the gap junction conductance in neural progenitors. (*B*) Magnified view of the indicated region in (*A*). (*C*) Bifurcation analysis of the cytosolic Ca^{2+} concentration in a nonpacemaker cell with the VGCC conductance (g_{VGCC}) as bifurcation parameter when g_{gap} = 200 μS/cm^2 and v_{gap} = 20 s^{-1}. Hopf bifurcations (HB) at g_{VGCC} = 18 μS/cm^2 and 25 μS/cm^2. (*D*) Magnified view of the indicated region in (*C*). (*E*) Bifurcation analysis of the cytosolic Ca^{2+} concentration in a pacemaker cell (blue) and a nonpacemaker cell (red) with the RyR Ca^{2+} permeability (v_{RyR}) as bifurcation parameter. (*F*) The effect on spontaneous Ca^{2+} oscillations upon Ca^{2+} influx inhibition in a pacemaker cell (top) and a nonpacemaker cell (bottom).

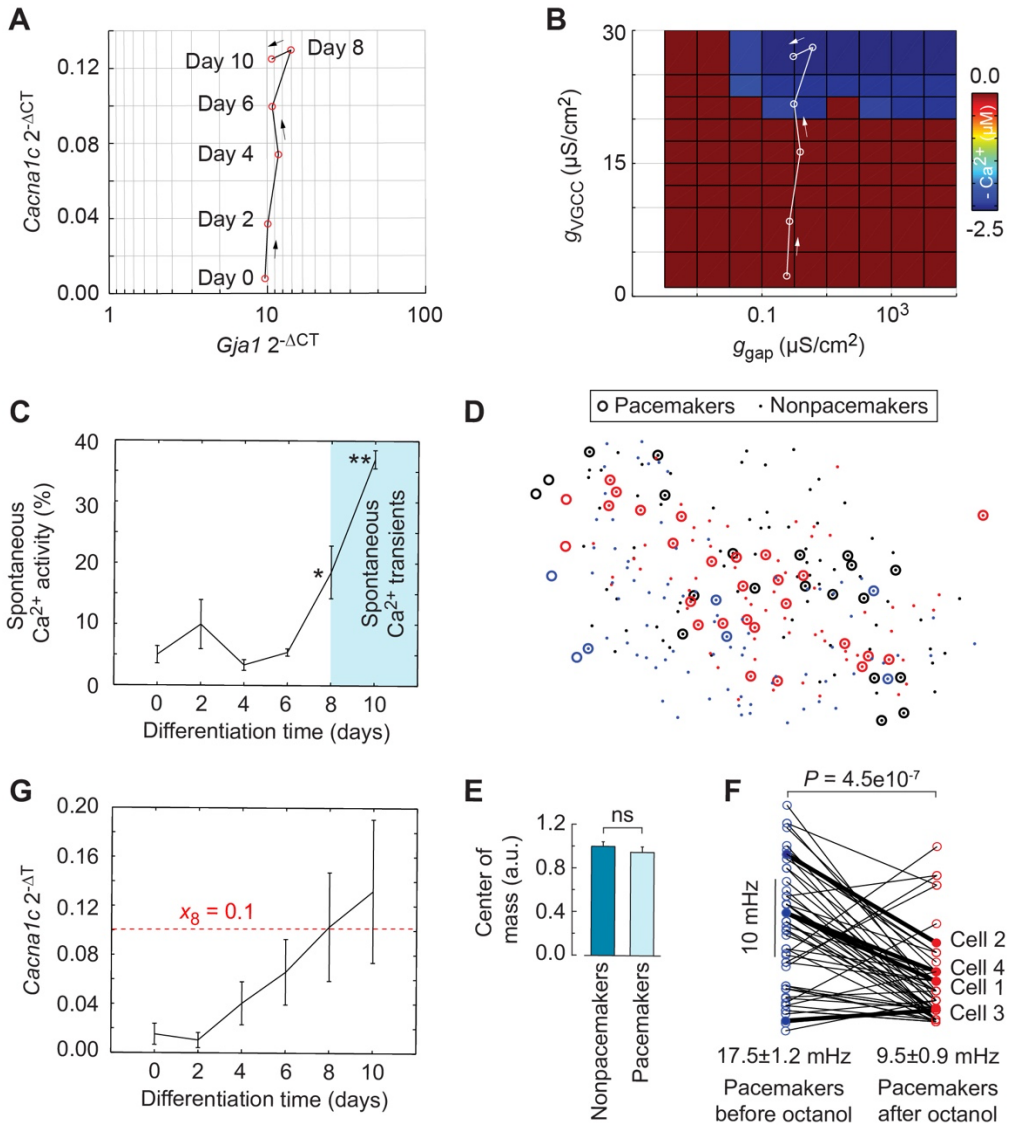

Fig. S4. Influence of *Cacna1c* expression on spontaneous Ca^{2+} activity in pacemaker and nonpacemaker cells. (*A*) Trajectory of differentiating embryonic stem (ES) cells based on the RT-qPCR measurements of *Cacna1c* and *Gja1*. The values are the mean expression of the connexin-43 gap junction gene *Gja1* (x-axis) and the $Ca_V1.2$ subunit gene *Cacna1c* (y-axis) at days 0 to 10 of differentiation. (*B*) Bifurcation analysis with the gap junction and VGCC conductances, g_{gap} and g_{VGCC}, respectively, as bifurcation parameters. The values are g_{gap} (x-axis) and g_{VGCC} (y-axis). The trajectory of the experimental measurements in (*A*) is superimposed onto the bifurcation surface plot. (*C*) The percentage of differentiating cells with spontaneous Ca^{2+} activity at days 0 to 10. The blue shaded area indicates significant spontaneous Ca^{2+} oscillations. (*D*) The spatial distribution of pacemaker cells (ring) and nonpacemaker cells (dots) in experiments on neural progenitor cells (N = 3). (*E*) The center of mass of the pacemaker (N = 3) and nonpacemaker (N = 3) cell populations in (*D*). (*F*) Frequency analysis of the spontaneous Ca^{2+} oscillations in pacemaker cells before and after gap junction inhibition with 1 mM octanol. (*G*) The expression of *Cacna1c* in differentiating ES cells for ten days. The expression level on day 8 is indicated x_8. The values are the mean ± s.e.m. The significance tests were calculated using unpaired (*C*, *E*) and paired (*F*) two-sided *t*-tests. $^*P < 0.05$, $^{**}P < 0.01$; ns, non-significant ($P > 0.05$).

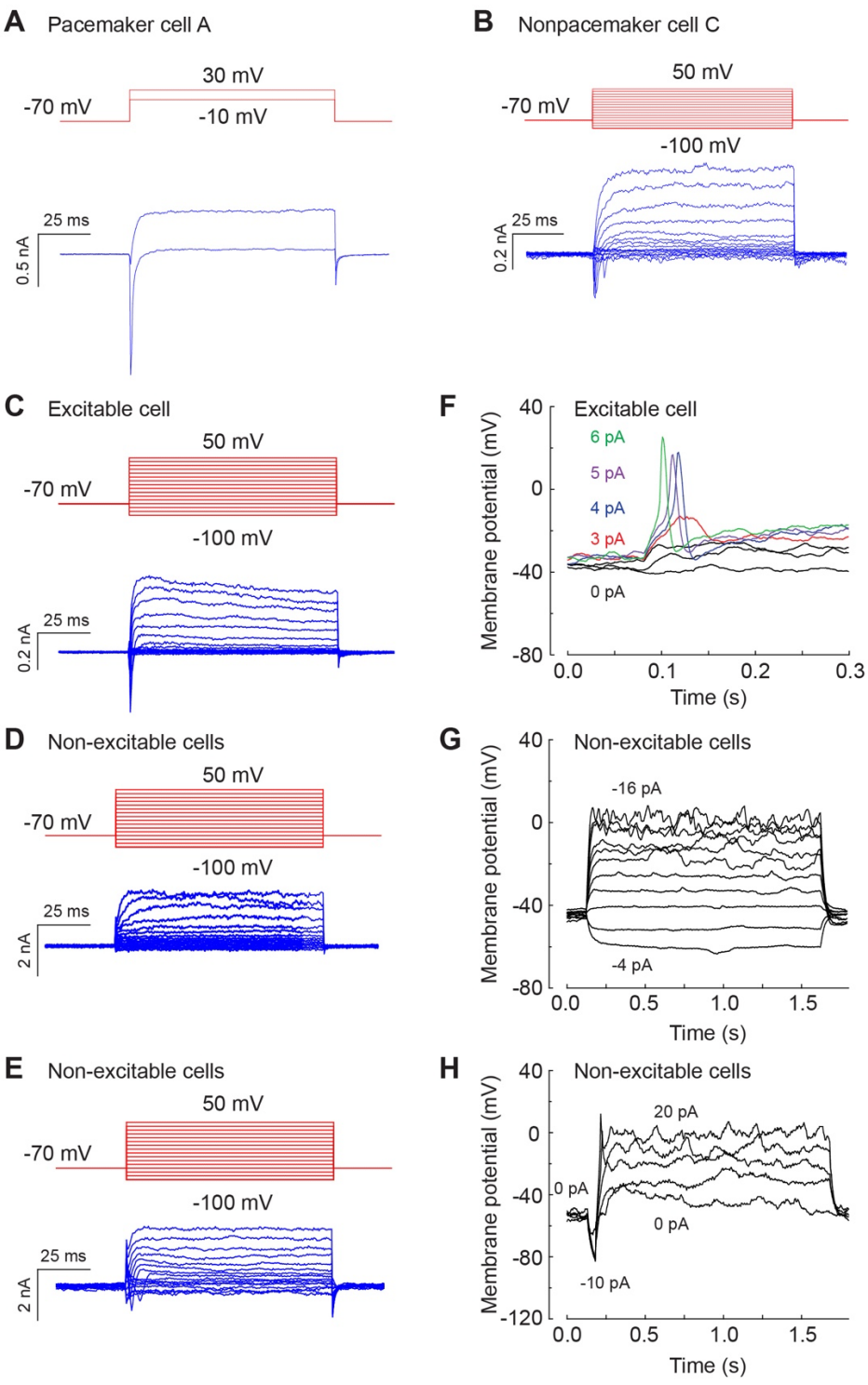

Fig. S5. Membrane potential responses in excitable and non-excitable cells. (*A* to *E*) Ion current recordings (voltage-clamp mode) upon application of rectangular voltage pulses in the pacemaker cell A of Fig. 4*B* (*A*) and nonpacemaker cell C of Fig. 4*E* (*B*), and in an excitable cell (*C*) and non-excitable cells (*D* and *E*). Red traces, applied rectangular voltage pulses. Blue traces, recorded currents. (*F* to *H*) Membrane potential recordings (current clamp mode) upon application of various currents in an excitable cell (*F*) and non-excitable cells (*G* and *H*).

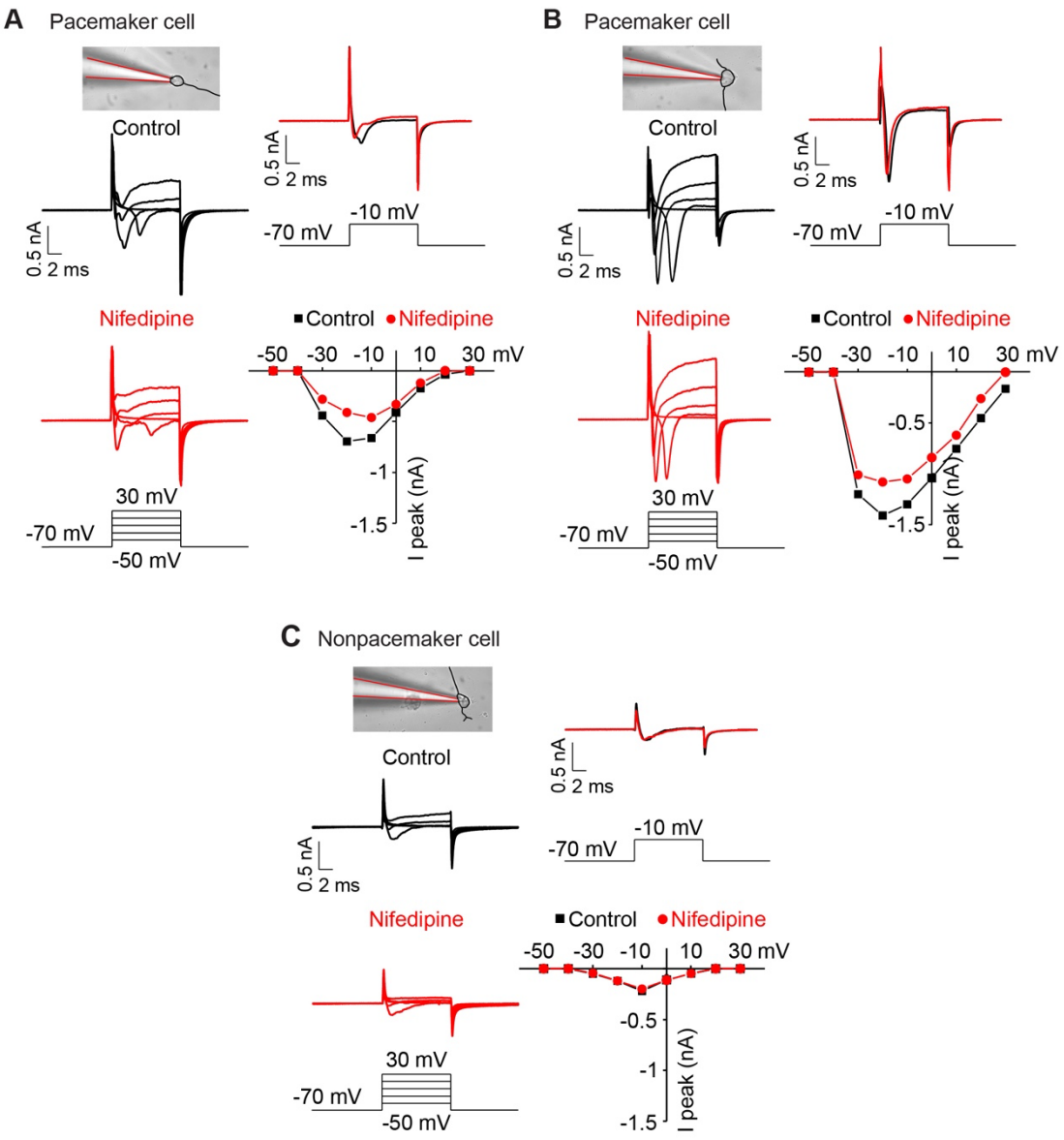

Fig. S6. Pacemaker cells but not nonpacemaker cells are sensitive to L-type VGCC blocker nifedipine. (*A* and *B*) Ion current recordings (voltage-clamp mode) in two pacemaker cells in absence (Control) or presence of 5 μM nifedipine. In each panel, top left photomicrographs showing the cell with the patch-pipette attached. Soma and processes are highlighted in black overlay. Bottom left, voltage steps from -50 to +30 mV from -70 mV holding potential. Top right, residual inward current upon a current step from -70 mV to -10 mV. Bottom right, relationship between voltage and current. Peak conductance is seen at around -20 mV, characteristic for L-type VGCCs. Data are a summary of observations for each cell individually. (*C*) Ion current recordings (voltage-clamp mode) in a nonpacemaker cell from the same culture as (*A*), in absence (Control) or presence of 5 μM nifedipine. Data are arranged as in the other panels. Note the insensitivity of the membrane conductance to nifedipine, as well as its peak at around -10 mV.

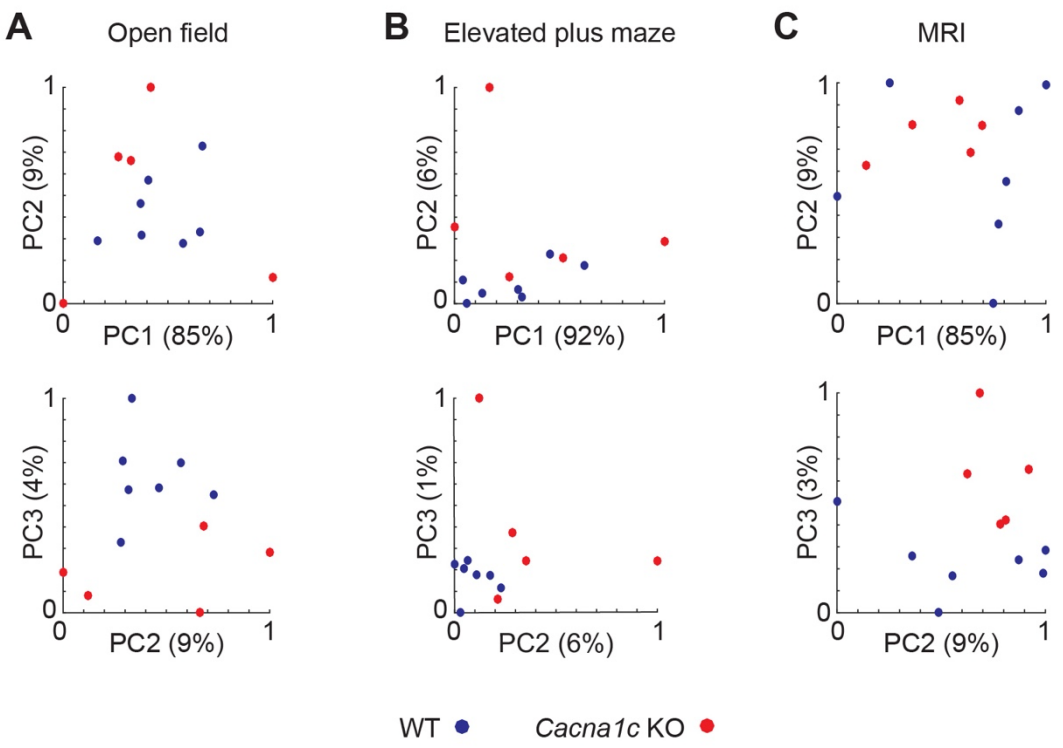

Fig. S7. Principal component analysis of the behavioral tests and MRI measurements. (*A* to *C*) Principal component (PC) analysis of the open field (*A*), elevated plus maze (*B*), and MRI (*C*) related variables for the WT (blue) and *Cacna1c* KO (red) mice. The percentages of total variance explained by the first three axes (PC1, PC2, and PC3) are given in parentheses.

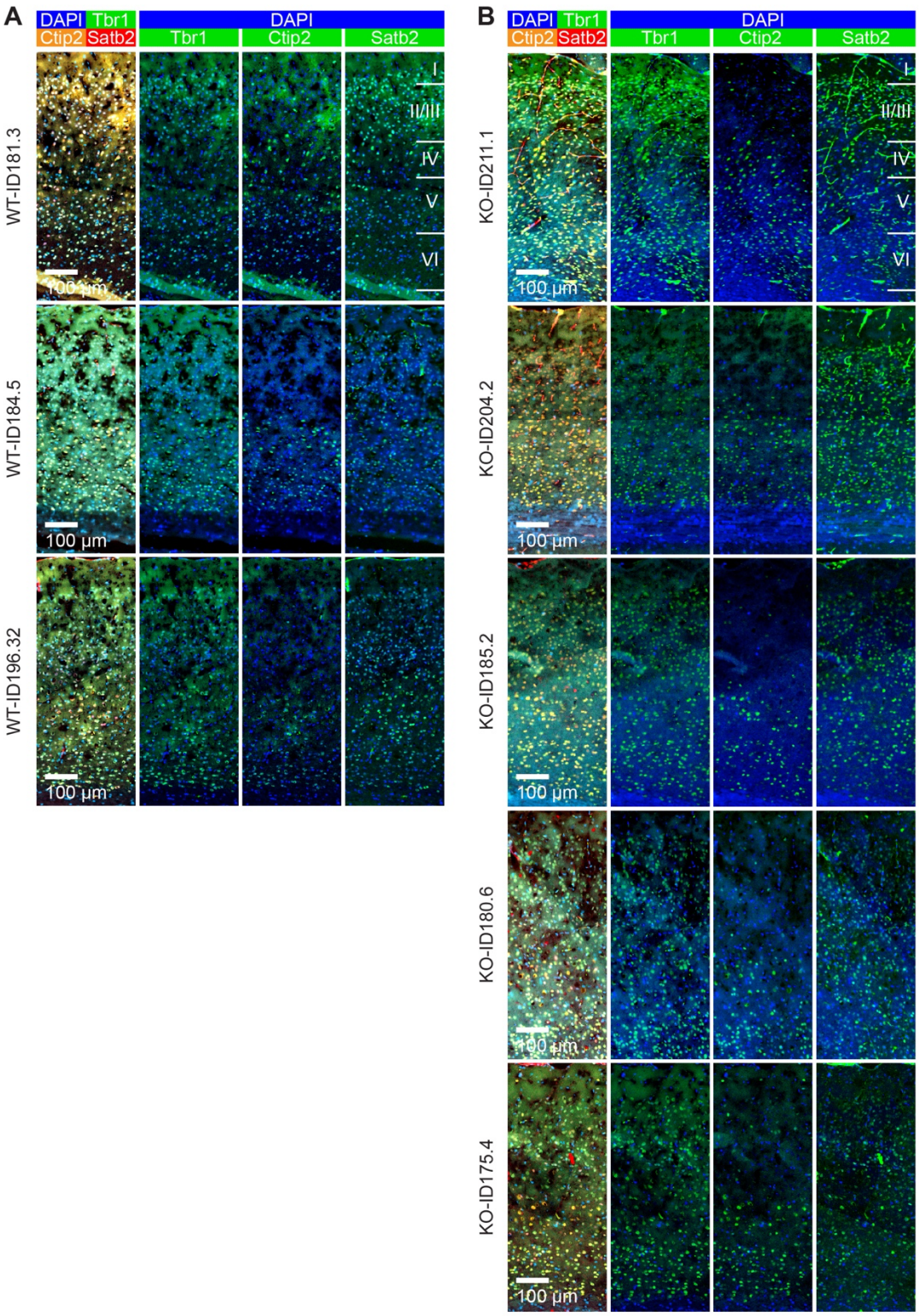

Fig. S8. Knockout of *Cacna1c* does not alter cortex layers in mice. (*A* and *B*) Immunohistochemistry images of the somatosensory cortex in WT (*A*, *n* = 3) and *Cacna1c* KO (*B*, *n* = 5) mice. Somatosensory cortex was stained with Tbr1, Ctip2 and Satb2. Nuclei were detected using DAPI. The mouse identification numbers are indicated. Scale bars, 100 µm.

Supplementary Tables

Variable	Value	Unit	Description	Reference
C_m	1	$\mu F/cm^2$	Membrane capacitance per area	(1)
I_{app}	0	nA/cm^2	Applied current per area	Bifurcation parameter, starting with no applied current
g_K	20	$\mu S/cm^2$	K^+ channel conductance per area	(1)
V_K	-85	mV	K^+ channel reverse potential	(1)
g_{Ca}	20	$\mu S/cm^2$	Ca^{2+} channel conductance per area	Bifurcation parameter, starting from (1)
V_{Ca}	120	mV	Ca^{2+} channel reverse potential	(1)
g_{gap}	200	$\mu S/cm^2$	Gap junction conductance per area	Bifurcation parameter
v_{gap}	20	$1/s$	Gap junction Ca^{2+} permeability	Bifurcation parameter
f_{cyt}	0.003 (<.01 in (1))	1	Buffering factor	Chosen
φ	12	$1/s$	Rate constant of K^+ channel	(1)
r	10	μm	Radius of cells	Chosen
F	96500	C/mol	Faraday's constant	(1)
v_{RYR}	5	$1/s$	RyR Ca^{2+} permeability	(1)
$v_{leak,ER}$	0.2	$1/s$	ER leak permeability	(1)
σ	0.02	1	Ratio of effective ER and cytosol volumes	(1)
V_1	-3	mV	Ca^{2+} channel parameter, activation voltage	(1)
V_2	30	mV	Ca^{2+} channel parameter, voltage width	(1)
V_3	-20	mV	K^+ channel parameter, activation voltage	(1)
V_4	30	mV	K^+ channel parameter, voltage width	(1)
$v_{max,PMCA}$	17 (> 5 in (1))	$\mu M/s$	Maximum transport rate	Chosen
$K_{1/2,PMCA}$	0.6	μM	Affinity for Ca^{2+}	(1)
$v_{max,SERCA}$	100	$\mu M/s$	Maximum transport rate	(1)
$K_{1/2,SERCA}$	0.2	μM	Affinity for Ca^{2+}	(1)
K_a	0.4	μM	RyR parameter	(1)
K_b	0.6	μM	RyR parameter	(1)
K_c	0.06 (< 0.1 in (1))	1	RyR parameter	Chosen

Table S1. Parameters used for mathematical modeling. Mathematical parameters and experimental values used in the computational model.

Supplementary Movie legends

Movie S1 (separate file). Magnetic resonance imaging in axial view. Visualization of the atlas-based segmentation of one adult mouse brain in axial view. Each color corresponds to one of the 39 segmented regions.

Movie S2 (separate file). Magnetic resonance imaging in coronal view. Visualization of the atlas-based segmentation of one adult mouse brain in coronal view. Each color corresponds to one of the 39 segmented regions.

Movie S3 (separate file). Magnetic resonance imaging in sagittal view. Visualization of the atlas-based segmentation of one adult mouse brain in sagittal view. Each color corresponds to one of the 39 segmented regions.

SI References

1. M. E. Fall CP, Wagner JM and Tyson JJ, *Computational Cell Biology*, Interdisciplinary Applied Mathematics (Springer, 2002), vol. 20, pp. 468.
2. J. Keizer, L. Levine, Ryanodine receptor adaptation and Ca2+(-)induced Ca2+ release-dependent Ca2+ oscillations. *Biophysical journal* **71**, 3477-3487 (1996).
3. S. Malmersjo *et al.*, Neural progenitors organize in small-world networks to promote cell proliferation. *Proceedings of the National Academy of Sciences of the United States of America* **110**, E1524-1532 (2013).
4. T. D. Helton, W. Xu, D. Lipscombe, Neuronal L-type calcium channels open quickly and are inhibited slowly. *J Neurosci* **25**, 10247-10251 (2005).
5. Y. A. Kuznetsov, *Elements of applied bifurcation theory* (Springer Science & Business Media, 2013), vol. 112.
6. M. Breakspear *et al.*, A unifying explanation of primary generalized seizures through nonlinear brain modeling and bifurcation analysis. *Cereb Cortex* **16**, 1296-1313 (2006).
7. E. M. Izhikevich, Nural excitability, spiking and bursting. *International Journal of Bifurcation and Chaos* **10**, 1171-1266 (2000).
8. F. A. Haight, *Handbook of the Poisson distribution* (Wiley, 1967).